Ultrasonics Sonochemistry 77 (2021) 105697

Contents lists available at ScienceDirect

Ultrasonics Sonochemistry

journal homepage: www.elsevier.com/locate/ultson

In-situ synchrotron X-ray imaging of ultrasound (US)-generated bubbles: Influence of US frequency on microbubble cavitation for membrane fouling remediation

Masoume Ehsani [a], Ning Zhu [b], Huu Doan [a,*], Ali Lohi [a], Amira Abdelrasoul [c,d,*]

[a] Department of Chemical Engineering, Ryerson University, 350 Victoria St., Toronto, ON M5B 2K3, Canada
[b] Canadian Light Source, Saskatoon, SK S7N 2V3, Canada
[c] Department of Chemical and Biological Engineering, University of Saskatchewan, 57 Campus Drive, Saskatoon, SK S7N 5A9, Canada
[d] Division of Biomedical Engineering, University of Saskatchewan, 57 Campus Drive, Saskatoon, SK S7N 5A9, Canada

ARTICLE INFO

Keywords:
Synchrotron X-ray imaging
Ultrasound (US)irradiation
Bubble cavitation
Ultrasound (US) frequency
Microbubble characteristics

ABSTRACT

Gaining an in-depth understanding of the characteristics and dynamics of ultrasound (US)–generated bubbles is crucial to effectively remediate membrane fouling. The goal of present study is to conduct *in-situ* visualization of US-generated microbubbles in water to examine the influence of US frequency on the dynamics of microbubbles. This study utilized synchrotron in-line phase contrast imaging (In-line PCI) available at the biomedical imaging and therapy (BMIT) beamlines at the Canadian Light Source (CLS) to enhance the contrast of liquid/air interfaces at different US frequencies of 20, 28 and 40 KHz at 60 Watts. A high-speed camera was used to capture 2,000 frames per second of the bubble cavitation generated in water under the ultrasound influence. Key parameters at the polychromatic beamlines were optimized to maximize the phase contrast of gas/liquid of the microbubbles with a minimum size of 5.5 μm. ImageJ software was used to analyze the bubble characteristics and their behavior under the US exposure including the microbubble number, size, and fraction of the total area occupied by the bubbles at each US frequency. Furthermore, the bubble characteristics over the US exposure time and at different distances from the transducer were studied. The qualitative and quantitative data analyses showed that the microbubble number or size did not change over time; however, it was observed that most bubbles were created at the middle of the frames and close to the US field. The number of bubbles created under the US exposure increased with the frequency from 20 kHz to 40 kHz (about 4.6 times). However, larger bubbles were generated at 20 kHz such that the average bubble radius at 20 kHz was about 6.8 times of that at 40 kHz. Microbubble movement/traveling through water was monitored, and it was observed that the bubble velocity increased as the frequency was increased from 20 kHz to 40 kHz. The small bubbles moved faster, and the majority of them traveled upward towards the US transducer location. The growth pattern (a correlation between the mean growth ratio and the exposure time) of bubbles at 20 kHz and 60 W was obtained by tracking the oscillation of 22 representative microbubbles over the 700 ms of imaging. The mean growth ratio model was also obtained.

1. Introduction

In recent years, membrane separation has been widely used in so many purification processes. Among all challenges that membrane-based separation processes confront, membrane fouling is one of the major drawbacks since it affects both the filtration performance and membrane lifetime. Ultrasound (US) cleaning technique has been proven to be an innovative and promising approach for fouling remediation and restoring the initial permeate flux [1–5].

In the presence of ultrasonic wave propagation inside a liquid medium, compression and rarefaction cycles frequently occur, having

Abbreviations: ABI, Analyzer based imaging; BMIT, Biomedical imaging and therapy; BM, Bending magnet; CLS, Canadian light source; FOV, Field of view; PCI, Phase contrast imaging; PC, Polycarbonate; SDD, Sample-to-detector distance; US, Ultrasound.

* Corresponding authors at: Department of Chemical Engineering, Ryerson University, 350 Victoria St., Toronto, ON M5B 2K3, Canada (H. Doan) & Department of Chemical and Biological Engineering, University of Saskatchewan, 57 Campus Drive, Saskatoon, SK S7N 5A9, Canada (A. Abdelrasoul).
E-mail addresses: hdoan@ryerson.ca (H. Doan), amira.abdelrasoul@usask.ca (A. Abdelrasoul).

https://doi.org/10.1016/j.ultsonch.2021.105697
Received 24 June 2021; Received in revised form 21 July 2021; Accepted 26 July 2021
Available online 5 August 2021

Nomenclature

A	Bubble area
c_w	Speed of the ultrasound wave
f_r	Resonance frequency
I	Ultrasound power intensity
P_A	Pressure amplitude of the ultrasound wave
R	Bubble radius
R_0	Resonance radius
$Ravg$	Average bubble radius
ρ	Density
γ	Specific heat ratio

physical, chemical, and thermal influences on the filtration system. Acoustic streaming caused by US irradiation helps create a convective current within the liquid and breaks the fouling layer. Bubble cavitation is another interesting phenomenon that occurs under US exposure and is mainly responsible for surface cleaning [6]. Bubble oscillation or explosion may cause an eddy current and shear force, breaking the fouling layer and dislodging the particles from the membrane surface. Small bubbles may also act as microstreamers, attaching to the particles and clear them away from the surface. The number of bubbles created under the US irradiation and their growing size are directly affected by the operational parameters such as US power intensity, US frequency, and liquid viscosity [7–9]. Changes in the number and size of the bubbles in turn bring about the variation of energy released to the medium through the bubble explosion. Therefore, a detailed knowledge of the influence of operational parameters on bubble generation and bubble dynamics would provide a thorough understanding of the mechanism and effectiveness of bubble cavitation on fouling remediation.

Several characterization techniques have been used for direct observation of cavitation activities and analyzing the bubble behavior under the US exposure. The optical methods are among those techniques employed to detect the physical and chemical responses; in addition to monitoring the microbubble dynamics by high-speed photography. These methods are more favorable for in vitro systems and the camera used for imaging has a limited depth of field. However, it is infeasible to capture all microbubbles created in the system [10,11]. Another commonly used technique is acoustic detection, including both the passive and active cavitation detection methods, and relying on acoustic emission through the bubble explosion or the impact of acoustic waves [12]. Thus, bubble cavitation, acoustic intensity, and acoustic field can be monitored by this technique. This technique can be used for *in vivo* systems. The timing and emission amplitude of bubble cavitation is influenced by the initial bubble size and US amplitude [10]. However, a limitation of this method is that no images from water medium and bubble cavitation are generated through the detection processes; as such, it is impossible to determine the number and size of the microbubbles in the system [13]. Scattering methods are also used for cavitation measurements either by laser scattering of single bubbles or by Synchrotron X-ray imaging [14]. For laser scattering of single bubbles, this method is only applicable to spherical bubbles; however, various microbubbles, spherical or non-spherical, are created within the acoustic field.

Compared to all those aforementioned characterization techniques, Synchrotron X-ray imaging is a non-destructive technique, working based on capturing the beam transmitted either from the microbubbles or the liquids surrounding them [15]. X-ray based images have high spatial and temporal resolution, which offer thorough information on the number and size of the bubbles created within the liquid medium. In this method, bubble cavitation is characterized based on the X-ray absorption [16]. The differentiation of molecular absorption and refractive index caused a visible boundary between the microbubbles and the surrounding liquid [17,18]. In recent years, the Synchrotron based X-ray imaging technique has been employed in several studies for *in situ* observation of acoustic field, cavitation region and bubble dynamics under the US exposure [19–26]. For investigating the effect of US irradiation on bubble formation and growth, Xu et al.[27] and Huang et al. [28] reported the measurement of bubble growth pattern and size distribution in the Al-Cu alloy by adopting the X-ray imaging technique and *in situ* visualization of the molten aluminum alloy-microbubble system.

In this study, the influence of US frequency on the characteristics and dynamics of cavitational bubbles and their application on membrane fouling remediation via real time visualization in the membrane feed compartment was investigated. A non-destructive scattering technique, synchrotron in-line PCI, was employed for high-speed imaging and bubble monitoring. The image contrast of liquid/air interface was improved, which is beneficial for the qualitative and quantitative analysis of bubble cavitation within the system. ImageJ software was used to analyze the images and determine the number and size of the cavitational bubbles at different US frequencies. Bubble characteristics at different time intervals and distances from the US transducer were also studied. The bubble size distribution plots, as well as the bubble velocity at different US frequencies, were obtained. Bubble growth pattern for the US-generated microbubbles at the US frequency of 20 kHz was also determined.

2. Synchrotron X-ray imaging for *in- situ* visualization of ultrasound-induced microbubbles

Compared to other imaging techniques, synchrotron-based X-ray imaging techniques available at the Bio-Medical Imaging and Therapy (BMIT) beamlines at the Canadian Light Source (CLS), located in Saskatoon, SK, Canada, were able to facilitate *in situ* investigation and real-time visualization of stationary and moving microbubbles in water inside the filtration unit and over the surface of the membrane, which is crucial in our study.

2.1. Phase contrast imaging (PCI) and Analyzer-based imaging (ABI)

Among different synchrotron X-ray imaging techniques, X-ray phase contrast imaging (PCI) and analyzer-based imaging (ABI) are able to detect the microbubbles. ABI has been demonstrated to provide high visibility of microbubble details with a good contrast compared to normal X-ray absorption techniques, in which microbubbles are invisible. ABI is a phase-sensitive imaging technique with the ability to detect subtle projected density variations. In ABI, a very bright and highly collimated X-ray beam is sent toward the cavitation field where small structures such as microbubbles refract and scatter the X-rays through small angles. Those small angles create contrast based on the very narrow reflectivity curve of the analyzer crystal. As the X-ray travels through the filtration unit thickness, it may be refracted, scattered, or absorbed. The refracted and scattered X-ray beams are collected at the detector behind the unit. The bubbles of a transient nature provided sufficient contrast to be imaged in a time-averaged exposure. For example, a single bubble with the same size as a detector pixel typically generates ~ 20% contrast compared to a region not containing a bubble. However, microbubble contrast agents are commonly used to improve ultrasound imaging of microbubbles, which act as an X-ray lens, with individual microbubbles refracting and a population of them scattering the X-rays. In addition, using ABI, the density of stationary and moving bubbles can be indirectly inferred by measuring the ultra-small angle X-ray scattering distribution in the region where bubbles are formed. However, at the top or peak location of the analyzer, there is a distinct loss of intensity due to scattering from the bubbles. The analyzer at the peak setting is sensitive to scatter and removes it from the image.

PCI, relies on the same sources of contrast within the object as with ABI; however, this method is somewhat different and simpler. In PCI, when the X-ray beam passes through a sample, changes occur in the

phase of the X-ray beam; even nano structures could produce phase contrast clearer than absorption contrast. In addition, information about the beam's phase shift caused by the sample is transformed into intensity variations and is recorded by the detector, as shown in Fig. 1. Because the X-ray phase shift can be quite high, PCI is very sensitive to density changes in the sample compared to conventional transmission-based X-ray imaging. In addition, PCI technique provided real-time imaging of stationary and moving bubble formation. Therefore, in this study PCI enables quantification of microbubbles for both phase-retrieved images achieved by processing multiple frames and also by "single-shot" images. PCI could quantitatively examine the number, size, and velocity of microbubbles suspension and provideing the basis for a dynamic imaging technique. It was demonstrated that PCI has significant utility with respect to detecting and visualizing microbubbles/cavitation bubbles.

2.2. *In-line phase contrast imaging (In-line PCI) optimization*

X-ray in-line phase contrast imaging (In-line PCI) is one of the phase contrast-based imaging techniques that require an X-ray source with some degree of transverse coherence. This coherence can be achieved by either having a small source size and/or the source can be placed far from the object and detector. The distance between the object and detector is used to adjust the level of phase contrast and its sharpness. Increasing the distance provides better phase contrast but at the expense of lower spatial resolution.

As shown in Fig. 2, X-rays passing through a junction between two different materials are refracted slightly, leading to changes in the X-ray wave front that propagate over this increased distance. The influence is captured in the image where the interfaces between materials of different X-ray refractive index are highlighted by bright and dark fringes due to regions of high and low apparent X-ray absorption on the detector. The width of these lines is dependent on the propagation distance between the object and the detector, and by varying this distance the width of these lines can be optimized to show a bright, easily distinguishable border. The phase produced is capable of generating significantly enhanced contrast, which decreases less rapidly with increasing energy than absorption contrast. As a result, the detection of interfaces between gas/liquid phases of different refractive indices is enhanced without increased dose. Therefore, the in-line phase contrast was used in our study to achieve high phase contrast of gas/liquid of the bubbles as the optimum synchrotron X-ray Imaging technique to facilitate real-time visualization of stationary and moving microbubbles in water.

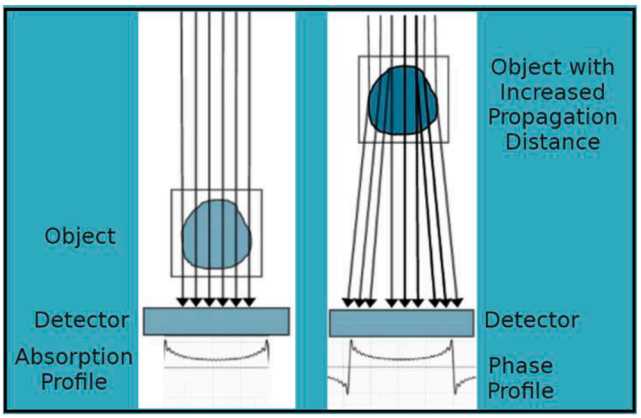

Fig. 2. Differences in detector response using in-line phase contrast imaging.

3. *In situ* synchrotron imaging at CLS beamline hatch

All experiments were performed at the polychromatic bending magnet (BM) beamline of the 3rd-generation synchrotron facility at the CLS. In order to achieve *in situ* bubble high quality visualization and imaging with enhanced contract between air/liquid phases several key parameters were considered and optimized. Those critical parameters included the selected beam, energy, and detector settings, sample-to-detector distance (SDD) for in-line PCI imaging, camera and its speed, mode of imaging, in addition to the material and the design of filtration unit.

3.1. *Polychromatic beam for in-situ bubble visualization*

The polychromatic beam was used at the BMIT-BM-05B1-1 bending magnet beamline to conduct the experiments, using filtered white beam mode. The white beam achieved fast data acquisition due to the high photon flux provided at the spectrum beam. Therefore, the white beam enabled the high resolution and high-speed projections, which were able

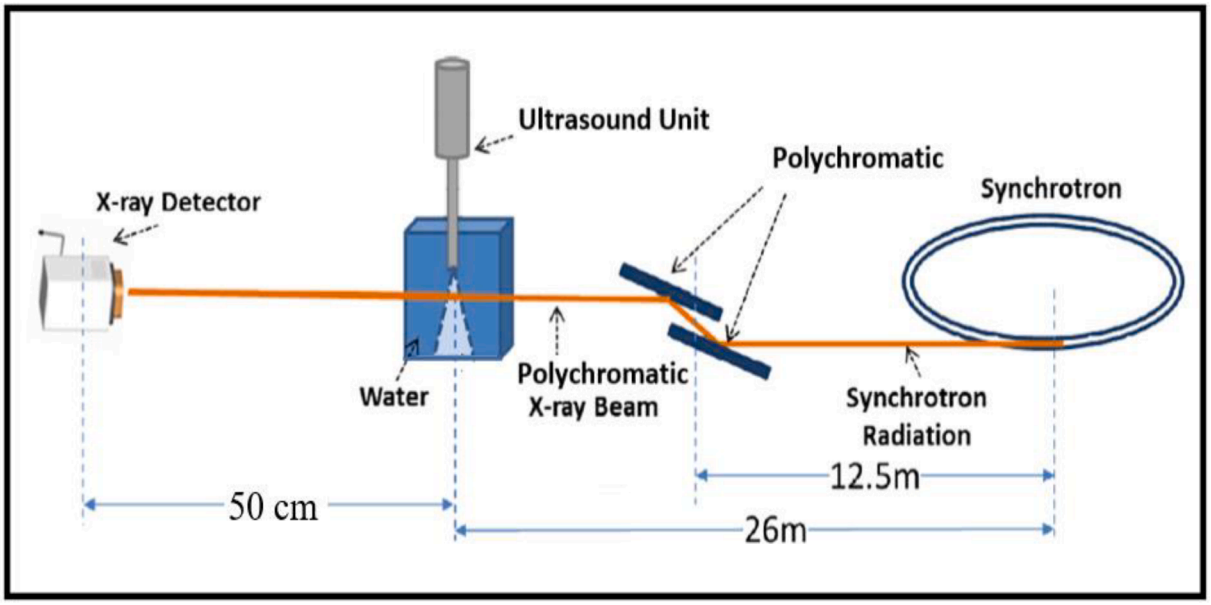

Fig. 1. Schematic diagram of the PCI setup at the CLS, which was used to image ultrasound-induced cavitation microbubbles in water medium.

to capture the bubbles and their dynamics with minimal motion artifacts in each scan. The advanced non-invasive imaging synchrotron in-line PCI technique was used to enhance the image contrast of liquid/gas interface, which is beneficial for the qualitative and quantitative analysis. During each scan, two thousand projections were captured in one second by the detector. With high flux, a typical high speed was achieved; and each projection was captured in 0.5 ms. The SDD of the in-line PCI technique of 50 cm was used during the experiments to obtain the best image contrast. X-ray radiographs were taken by a high-resolution high-speed detector camera (DIMAX HS4; PCO, Germany) combined with a beamline monitor (AA40; HAMAMATSU, Japan) with a pixel size of 5.5 μm and field of view (FOV) of 11 × 4 mm^2. The spatial resolution and FOV coverage of the detector are suitable for investigations of the number and size of bubbles generated by the ultrasound at different operating conditions. All of the experiments were performed at room temperature (22 °C) and a relative humidity of 35%. Details of parameters' optimization for enhancing the phase contrast are described in Section 3.2.

3.2. Optimization of photon flux for enhanced phase gas/liquid contrast

3.2.1. Optimum energy used

The synchrotron polychromatic beam of BMIT-BM 05B1-1 has a spectral energy of 20–50 keV. A sufficient flux of photons is needed to achieve high-quality imaging and phase contrast. A spectral energy setting was selected based on the radiation transmitted through the sample and pixel saturation values that achieved the best flux and imaging quality. As presented in Fig. 3, increasing the energy above 25 KeV resulted in slower imaging due to the lower photon flux. In our study, the beam was cut to a very small FOV size of ~ 40 × 5 mm^2 by a slit set to reduce X-ray white beam scattering. A photon flux of ~ 10^{13} photons/mm^2/s of white beam was used in this study.

3.2.2. Optimization of feed compartment design

The design of the filtration unit was the most challenging factor in the *in-situ* experiments of bubble imaging at CLS. Initially, a 4.5-mm thick polycarbonate (PC) was used to construct the feed compartment of the filtration unit. The aim was to avoid cracking due to the synchrotron radiation; however, the thickness resulted in blocking ~ 90% of the photon flux. A thinner 2-mm thick PC was then used to reduce absorption of the photons; however, this resulted in immediate cracking due to the radiation. The feed compartment material was then replaced with Lexan® polycarbonate (Dielectric Manufacturing, Wisconsin, Iowa, USA), which offers an excellent combination of toughness, dimensional stability, and heat and flame resistance. Lexan had a density of 1.19 × 10^3 to 1.2 × 10^3 kg/m^3, which allowed a sufficient photon flux transport for visualization of the microbubbles. It also has excellent creep resistance across a broad high temperature range. Lexan has a thermal expansion coefficient of 6 × 10^{-5} to 8 × 10^{-5} strain/°C and a specific heat capacity of 1.23 × 10^3 to 1.28 × 10^3 J/kg °C.

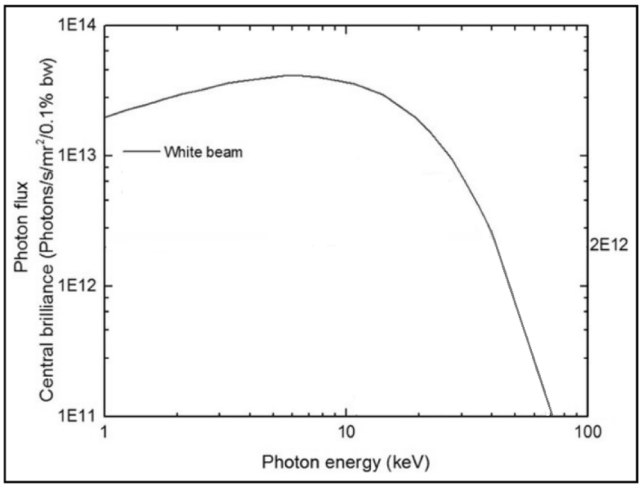

Fig. 3. Photon spectra vs. energy spectrum of white beam at the BMIT-BM 05B1-1 beamline.

In addition, the water-body thickness inside the feed compartment of the filtration unit, is an additional crucial parameter, as presented in Fig. 4. When the feed compartment width and the water channel were large (>20 mm), as presented in Fig. 4 (a), the water body in the chamber was too thick and absorbed/blocked over 99% of photons and prevented bubble visualization. A conical feed compartment was then designed and tested with the photon flux focused at a small water body with a thickness of 20 mm, while having the ultrasound influence on a wide area of the conical design, as presented in Fig. 4(b). For this design, the bubbles were trapped in the top section of the conical feed compartment, closer to ultrasound transducer; and hence, none of the bubbles were visualized, as shown in Figure S.1(a). Finally, a rectangular compartment unit was then designed with a water body thickness 20 mm and depth of 4 mm, as presented in Fig. 4 (c). The optimum design of Fig. 4 (c) allowed a high photon flux that was sufficient for the required contrast to visualize the bubbles, as shown in Figure S.1 (b). It is worth noting that although in both designs the beam was focused on a water body thickness of 20 mm, and the depth of water from the ultrasound transducer to the membrane surface was the same, the feed compartment shape had a great influence on the bubble visualization and the image quality, as presented in Figure S.1. Therefore, the design of the feed compartment is an important factor to achieve bubbles visualization and to maximize the photon flux, generated at a specific spectral energy of the beam, which results in enhanced quality of images.

Consequently, the appropriate material, water body thickness and the feed compartment design were critical parameters in this study and must be optimized to avoid cracking of materials, obtaining clear images of the bubble dynamics, and achieving high phase contrast of gas/liquid interface of the bubbles.

3.3. Optimization of in situ visualization and image quality

A higher speed camera (DIMAX HS4; PCO, Germany) combined with a beamline monitor (AA40; HAMAMATSU, Japan) with a 5.5-μm pixel size, LuAG scintillator, fast readout speed and 11 × 4 mm^2 FOV was used. A total of 4000 projections in 2 s (one image per 0.5 ms) were obtained. This setup was sufficient to capture the behaviour of bubbles and detect the bubble dynamics. The SDD was adjusted to maximize the phase contrast without penumbral blurring. The choice of SDD had to fall between 30 and 50 cm due to structural limitations of the BMIT hatch stage. Distances<50 cm had poor phase contrast and limited quality, as shown in Figure S.2 (a). An optimal SDD of 50 cm was chosen for the in-line PCI technique to obtain the best image contrast and resolution, as presented in Figure S.2 (b).

3.4. Ultrasound unit used

Ultrasonic device (ultrasound transducer, QXCT-20 (28) (40) 60 T-64HSP8, Quanxin, China), with specifications of 110 VAC, 60 Watts, and different frequencies (20, 28, 40 KHz), meeting the standards of the CLS inspection department. A schematic diagram of the membrane unit with the ultrasonic transducer employed for bubble imaging is presented in Fig. 5. The setup was mounted on the beamline rotating stage with a strong magnetic mount. The stage can be controlled to return to the same position and to achieve consistency in the images at different time intervals.

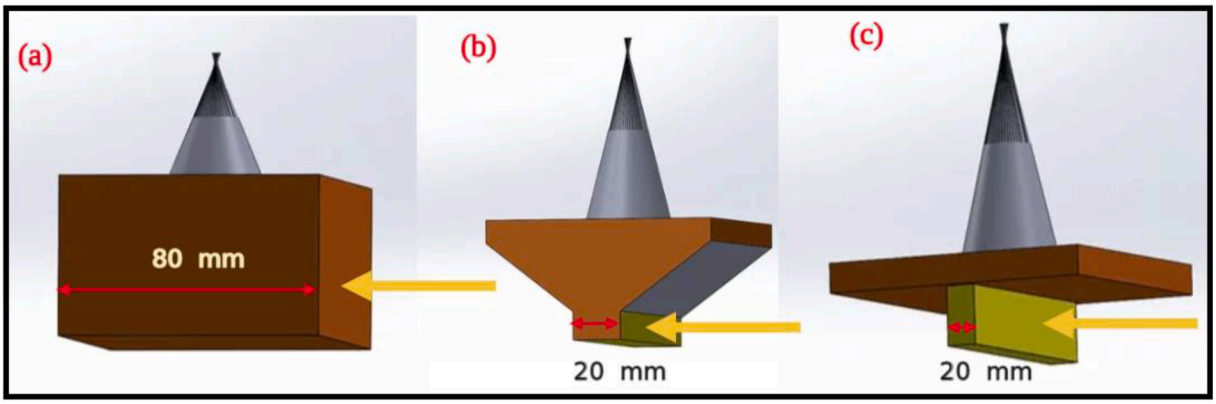

Fig. 4. Ultrasound feed compartment design optimization to enhance photon flux and bubble visualization.

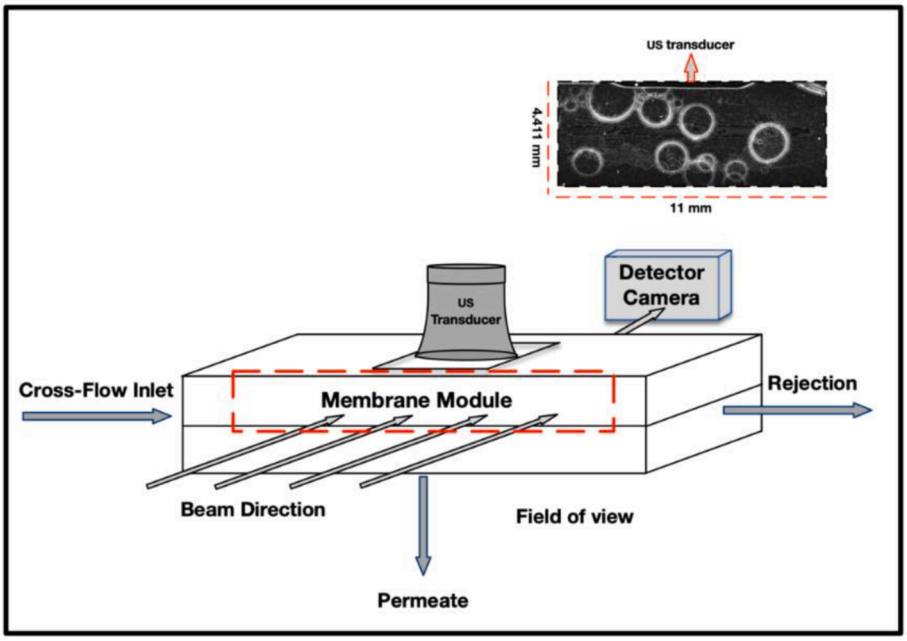

Fig. 5. Schematic diagram of the membrane module with ultrasonic transducer employed for bubble imaging at the feed compartment.

3.5. Image processing and analyses

3.5.1. Raw image calibration and processing

The imaging procedure was controlled from the control room just beside the imaging BMIT hatch at CLS. At the start and the end of the imaging process, dark-field images and flat-field images were also collected for each view. These were later used to make corrections to the collected tomographic projections prior to reconstruction by subtracting both dark projections and flat projections from original tomographic projections. Liquid tends to attenuate beam photons more and appears brighter in the images compared to air, which absorbs less energy. The images were segmented, where the phase densities were identified by tuning the threshold on the grey scale. Outlier removal was applied while selecting the threshold, which was calibrated while not over-modified to affect the image quality.

3.5.2. Microbubble analyzing approach and image processing by ImageJ

The number, size, and fraction of total area occupied by micro-bubbles (variation of density) were calculated at each US frequency of 20, 28, and 40 kHz (at constant US power of 60 W) by using the full-stack analysis. Afterward, to study the bubble formation and development at different time of imaging, all images (4000 frames, 2 s of imaging) were divided into 8 piles (pile of 500 frames, 0.25 s of imaging), and the average value of all those bubbles related parameters were measured for each pile. Thus, changes in the number, size, and variation of density were recorded over the US exposure time. In order to determine the bubble characteristics at different distances from the US transducer, all images (4000 frames per US frequency) were vertically divided into three identical slices, and the average value of all those bubble-related parameters were calculated for each individual slice. Fig. 6 shows the summary of microbubble analyzing approach.

The earliest frames provided by the high-speed camera were entirely dark with no bubbles, as shown in Fig. 7 (a). Following the removal of background noise, adjusting the threshold, and enhancing the brightness, the ultrasonic waves were then detected in filtered images. US wave in the liquid medium (blue) and the area of interest (yellow) for image processing by ImageJ software is depicted in Fig. 7 (b). The US transducer was placed at the top of the frame, and the area of interest was selected immediately below it (11.00*4.05 mm^2).

The grayscale images used to capture the cavitational bubbles were obtained using the ImageJ software after adjusting the filters. As mentioned earlier, the refractive index of cavitational bubbles is different from that of water. There could be some empty volumes (empty cavity/void) or bubbles filled with air, water vapor, or other dissolved

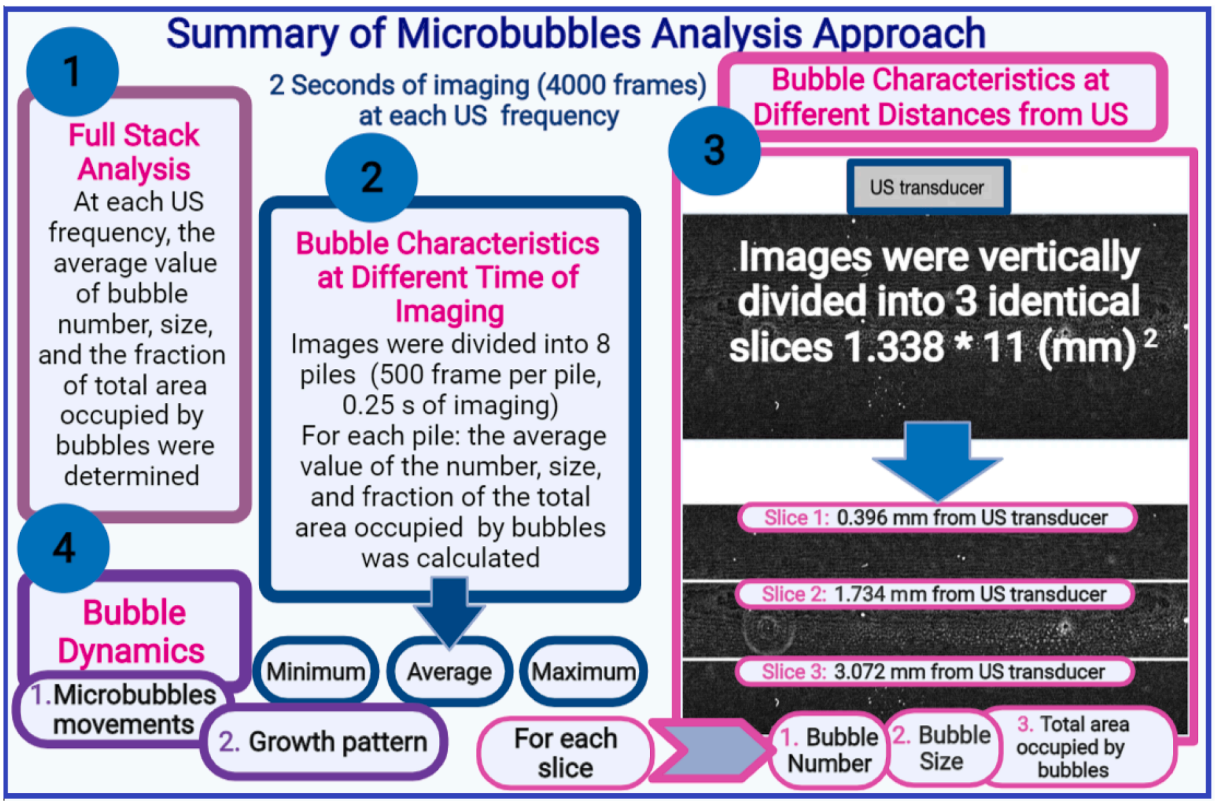

Fig. 6. Summary of microbubbles analysis approach.

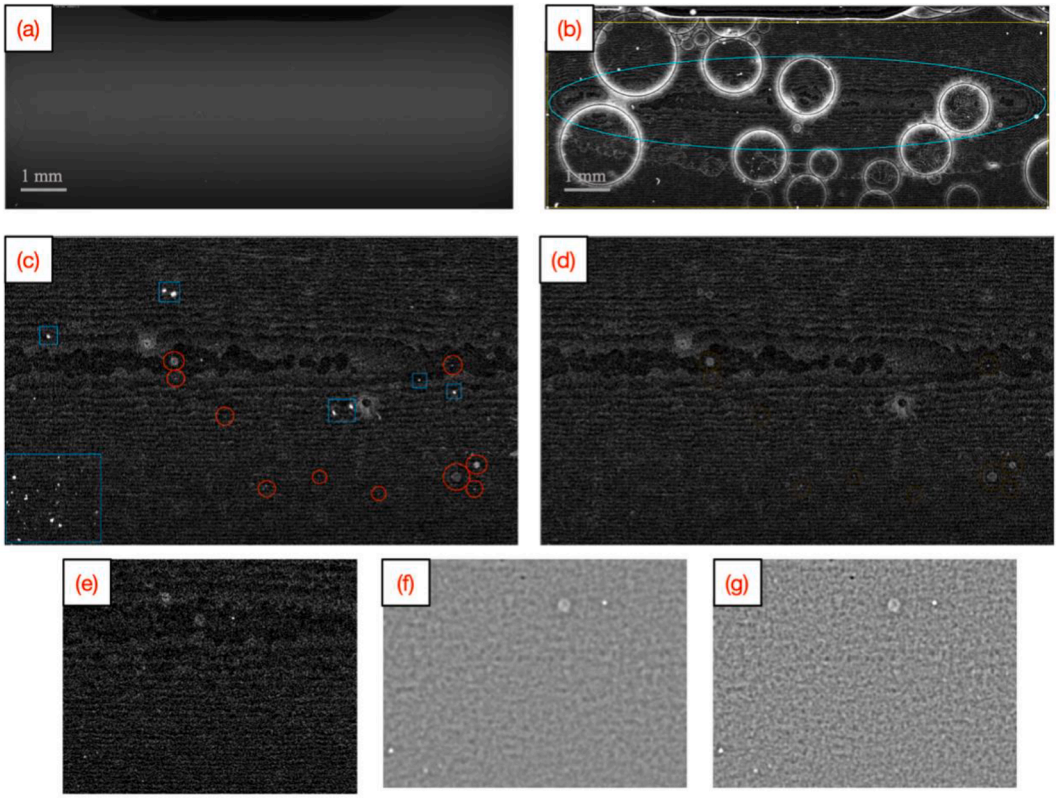

Fig. 7. a) Raw image generated from the high-speed camera at CLS, b) Area of interest for image analysis using ImageJ, c) Moving microbubbles and bright pixels, d) Outliner function for noise removal, e) Image after subtracting the background and increasing the brightness, f) Image after using the Bandpass Filter, g) Image after applying the Sharpen function.

gases. Thus, the X-ray beam transmitted to the liquid-bubble system is less attenuated by the cavities, resulting in a different grey color level than the water surrounding them. As shown in Fig. 7 (c) (red circles), the bubble–liquid boundary can be recognized by having different grey levels for cavities and water. Randomly bright pixels were also observed (blue squares, Fig. 7 (c) due to the X-ray scattering or defects of the scintillator. Thus, the remove-outliner function was employed to eliminate those bright pixels [29]. Fig. 7 (d) presents the effect of noise removal function on images. As it is evident, all bright pixels in Fig. 7 (c) are turned to a similar grey level of water medium.

In order to analyze the number and size of bubbles, the edge artifacts were reduced and the image quality was improved using the Bandpass filter. Next, the details of images were accentuated by adjusting the contrast with the Sharpen function. Fig. 7 also shows the final images after e) subtracting the background, f) using the Bandpass Filter, and g) applying the Sharpen function. By applying those functions on initial frames, the final images generated by ImageJ would be well prepared for changing the threshold and applying the Analyze function. The software detected all bubbles with the size of 0-infinity. However, bubbles on the edges of the frames were excluded from the calculation.

4. Results and discussion

4.1. Influence of US frequency on microbubble formation-Full stack analysis

The full-stack analyzing function was employed to investigate the influence of US frequency at 20 KHz, 28 KHz and 40 KHz on the creation of the cavitational bubble. Table 1 shows the average value for the number, size, and fraction of area occupied by microbubbles analyzed using ImageJ.

The results of image processing showed that more bubbles were created as the US frequency increased such that the number of bubbles at 40 kHz was about 808, while it was only about 176 at 20 kHz. However, larger bubbles created at lower frequency such that the average bubble radius at 20 kHz was about 6.8 times of that at 40 kHz. >22.0 % of the whole frame was occupied by bubbles created at 20 kHz; however, this value was only about 2.4 % at 40 kHz. According to this finding, large bubbles created at 20 kHz may cause the convective current formation, owing to their oscillation in water. Large bubbles may also release a substantial amount of energy into the surrounding after the explosion, creating turbulent flow and shear force near the membrane surface, resulting in the surface cleaning by breaking the fouling layer. On the other side, the high number of small bubbles created at 28 kHz or 40 kHz could act as microstreamers and help with particle detachments and membrane surface cleaning.

4.2. Microbubble formation at different time of imaging

Fig. 8 shows the averaged values for all bubble-related parameters at 0.25 s time intervals. All those parameters were measured at different imaging times to investigate the effect of the US exposure time on microbubble formation and its growing size. No significant changes in the number or size of the bubbles were observed during 2 s of imaging. All minor changes are attributed to the bubble explosions, bubble growth, and re-creation of bubble nuclei. Therefore, cleaning efficiency with the help of cavitational bubbles seems to be fairly constant during this period of time, which in favor for membrane fouling remediation applications.

Table 1
Average value for each parameter at different US frequency at 60 Watts.

US frequency	Average number of bubbles	Average bubble radius (μm)	Average variation of density (%)
20 kHz	176	135	22.5
28 kHz	793	20	2.2
40 kHz	808	20	2.4

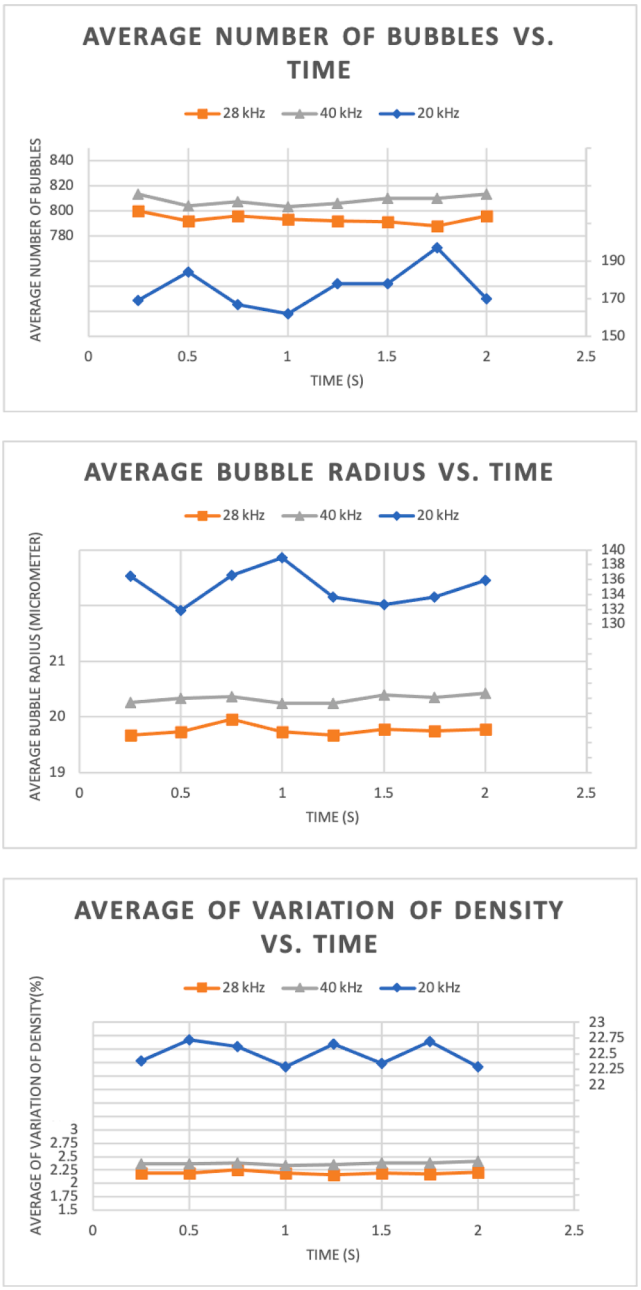

Fig. 8. The averaged value for each parameter during 2 s of imaging at the US frequency of 20 kHz, 28 kHz, and 40 kHz.

As it is evident from Fig. 8, there are always frames with the minimum, average, and maximum numbers of bubbles at different time intervals. The bubble size distributions for all those frames at US frequencies of 20 kHz, 28 kHz, and 40 kHz were analyzed using MATLAB. This was done to determine the ranges of the number and size of bubbles created at different time intervals at each US frequency, which may provide different effects on fouling removal. Fig. 9 shows the images with the minimum, average, and maximum number of bubbles, as well as the bubble size distribution of each frame under the US irradiation of 20 kHz, 28 kHz, and 40 kHz.

As shown in Fig. 9, it seems that the bubble size is more uniformly distributed at 28 kHz and 40 kHz, covering a broad range of bubble sizes from R = $1\mu m$ to almost 40 μm. On the other hand, the bubble size distribution plots for 20 kHz show a sharp peak at a small bubble size

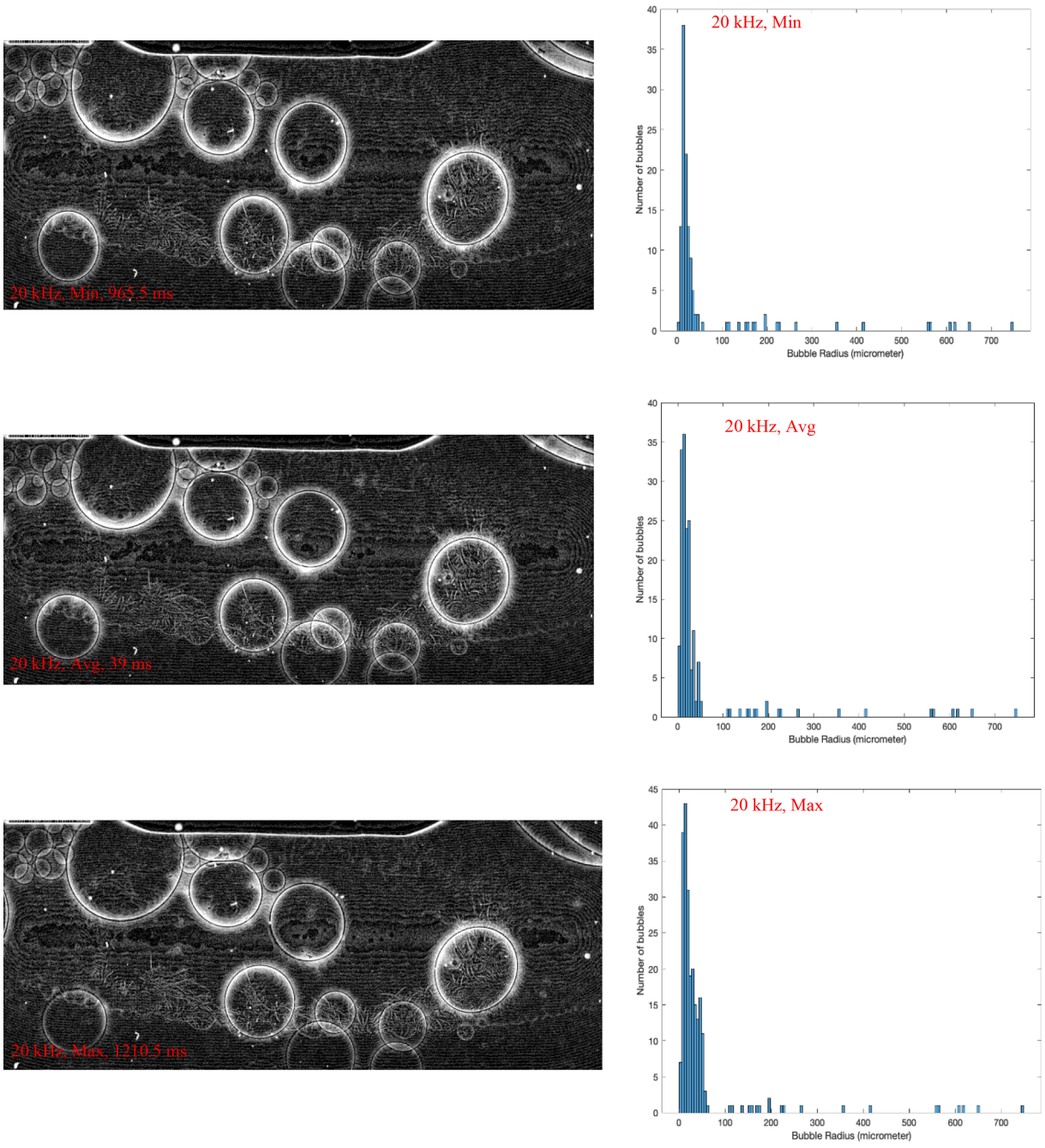

Fig. 9. Images with minimum, average, and maximum number of bubbles and bubble size distribution plots at different US frequencies.

range (R < 50 μm). However, the size distribution plots also show the presence of very large bubbles for all images with the minimum, average and maximum number of bubbles. In fact, there are a number of large bubbles with R = 100–600 μmoscillating at their stationary position and all other small bubbles populated at a bubble size smaller than 50μm.

The number, size, and fraction of area occupied by bubbles are summarized in Table 2. The average number of bubbles increased as the frequency changed from 20 kHz to 40 kHz. Nevertheless, an opposite trend of the averaged bubble size was observed where the averaged bubble size was smaller as the frequency increased from 20 kHz to 40 kHz. It is also interesting to mention that even the minimum area occupied by bubbles at 20 kHz is much larger than the maximum of those values at 28 kHz and 40 kHz. The minimum value for the average variation of density at 20 kHz was 22.2 % which is about 7.7 and 5.2 times of maximum values at 28 kHz and 40 kHz, respectively. The area occupied by bubbles reflects both the number and size of the bubbles. Therefore, using the US irradiation at 20 kHz appears to have the most effective result in fouling removal since microbubbles are sufficiently large to cause the convective current and form the turbulent flow by their explosion.

4.3. *Microbubble characteristics at different distances from the US transducer*

The distance of the liquid medium from the US transducer is another effective parameter that may influence bubble formation and growth. In this regard, all images were divided vertically into three slices to analyze the bubble characteristics at different distances from the transducer, as

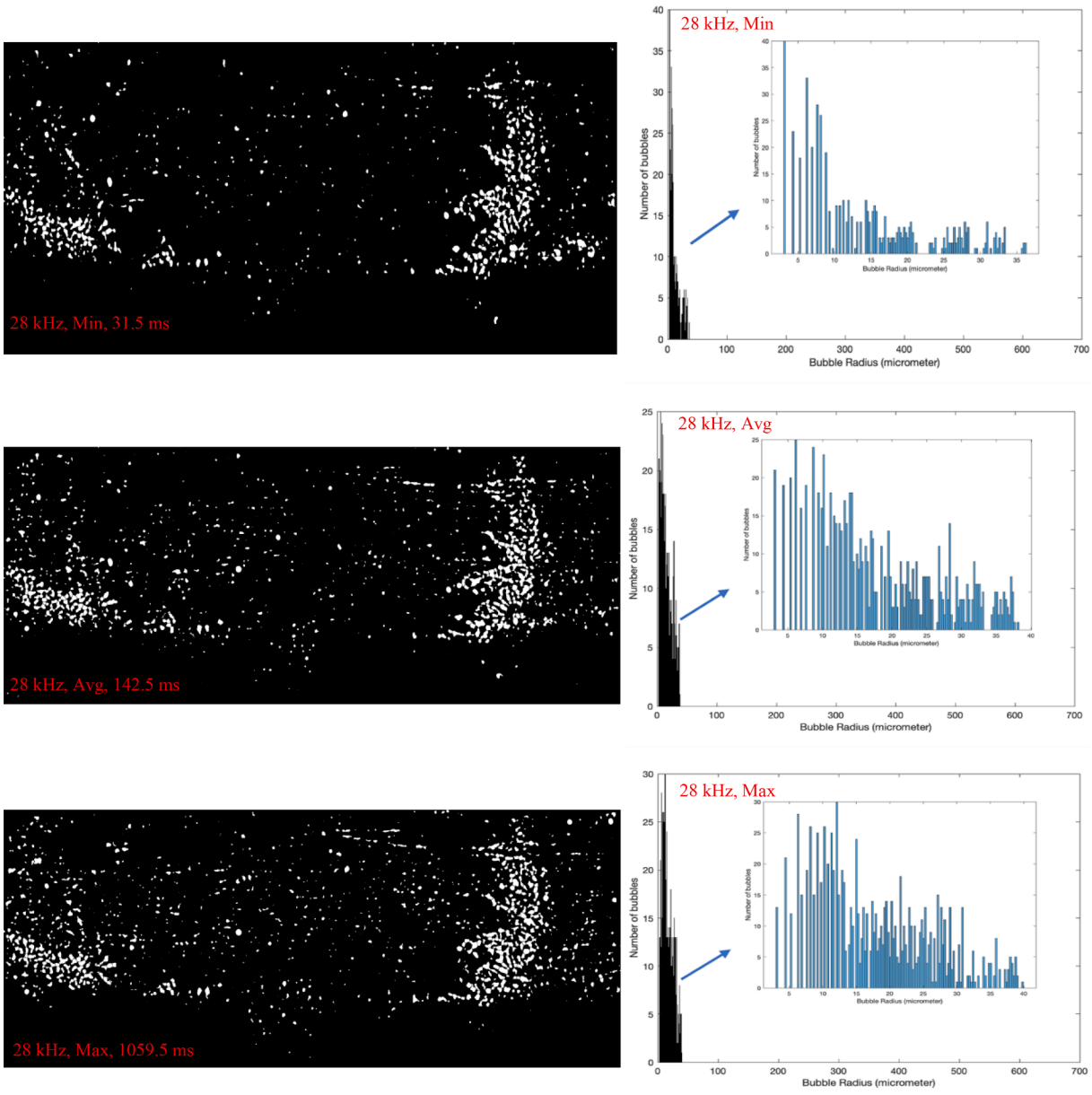

Fig. 9. (*continued*).

described in Section 3.5.2 and Fig. 6. The averaged values for all bubble-related parameters were calculated for each slice and at each US frequency. The summary of the results is presented in Table 3.

According to the results, it was observed that most bubbles were created in the middles slice and close to the US field. As mentioned earlier, the main purpose of using US irradiation is to take advantage of the microbubbles near the membrane surface. When the membrane is inserted into the system, there is almost a 2 mm gap between the membrane surface and the US transducer. The middle slice is at 1.7–3.0 mm apart from the transducer. Thus, the membrane would be placed somewhere in the middle slice locality, where both the US field and a population of microbubbles were observed. It was also noted that bubbles, captured in the middle slices, at US frequency of 28 kHz and 40 kHz were larger, which occupied more spaces compared to those at the top and bottom slices. However, the mean bubble size in the middle slice at 20 k Hz was lower than that of the top slice closer to the transducer; and it was attributed to the higher number of bubbles captured in the vicinity of US field; however, the area occupied by those bubbles were still more than that at other slices.

The variation of density or the fraction of total area occupied by bubbles represents both the averaged number and the size of the bubbles in each part. Regardless of the US frequency, bubbles created at the middle slices occupied the largest area, compared to those at the top or bottom slices. As presented in Table 3, the average variation of bubble density in the middle slice was about 7.7 %, 1.1 %, and 1.0 % at the US frequency of 20 kHz, 28 kHz, and 40 kHz, respectively. According to this finding, the area occupied by bubbles captured in the middle slice and under 20 kHz US irradiation was more than seven (7) times of those at 28 kHz and 40 kHz, which would likely cause a significant difference in membrane surface cleaning and more effective result in fouling remediation.

Bubble formation and growth in the middle slice and close to the membrane surface would help to dislodge the fouling layer. Results showed that a considerable number of bubbles were also captured at the top of the frames. If the number of bubbles at the middle slice was sufficient to dislodge the particles; then, bubbles at the top of the frames (slice 1, 0.396–1.734 mm away from transducer) would further help to clear them away from the surface and improve the fouling remediation.

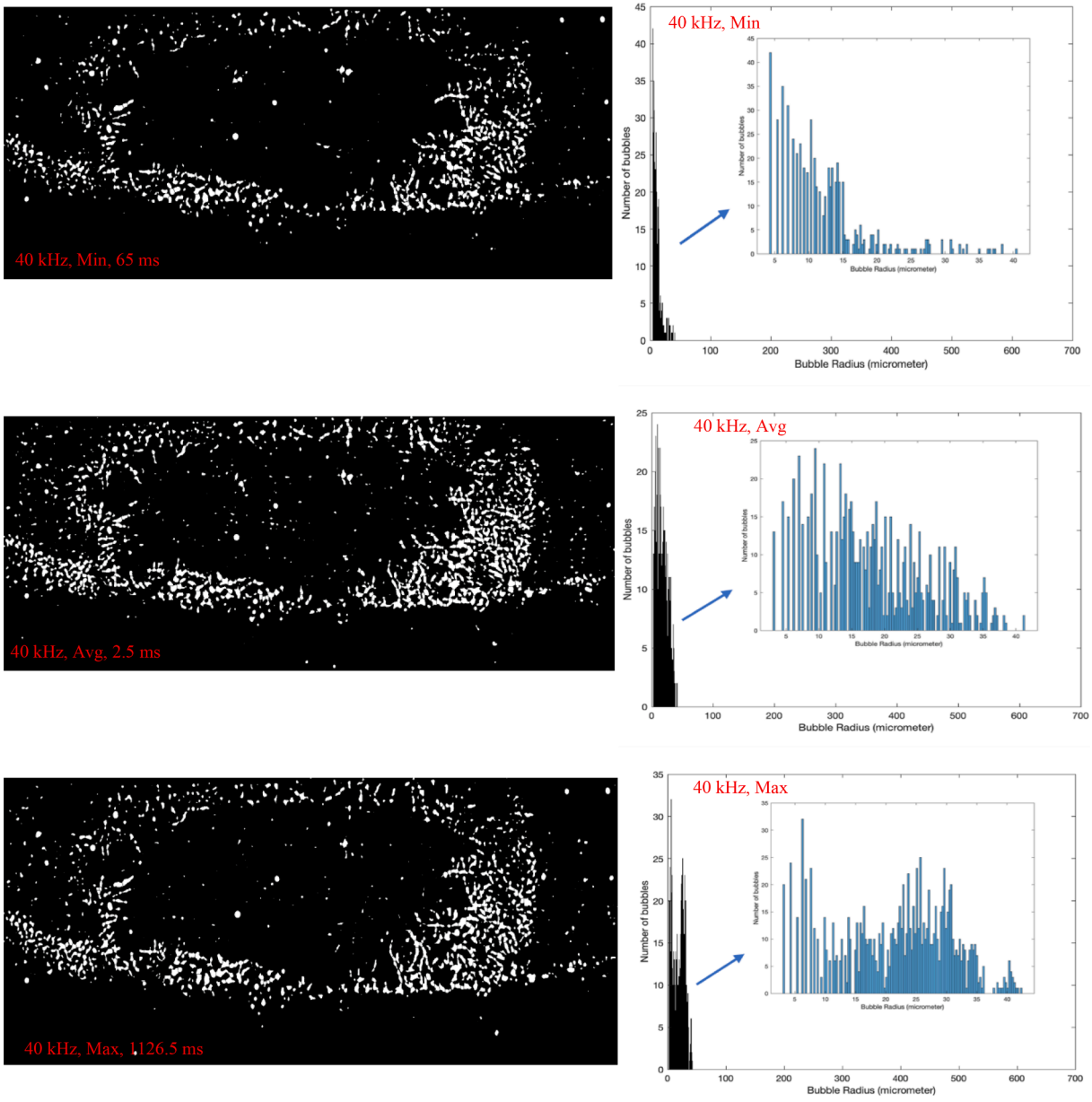

Fig. 9. (*continued*).

4.4. Dynamics of US-generated microbubbles

Microbubble cavitation includes several elementary processes such as bubble nucleation, growth, oscillation, movement, coalescence, splitting, and explosion under some conditions. In this section, the microbubble movement in water under the ultrasound irradiation has been comprehensively studied. Also, the microbubble growth pattern at 20 kHz is quantified such that a polynomial equation as a function of the bubble growth ratio and time can be determined. Cavitational bubbles can be stationary microbubbles or travelling through the liquid medium. In this study, microbubbles created at 28 kHz and 40 kHz were too small to track their oscillation and development patterns. In addition, small bubbles mostly traveled upward quickly and disappeared in the vicinity of the US transducer. So, it was very challenging to track the number of bubbles in the long run to quantify the growth pattern. On the other hand, a limited number of bubbles (22 bubbles) at 20 kHz were selected since their size and lifetime were sufficient to be tracked for a period of time.

4.5. Microbubbles' travel in water

Bubbles behave differently and have non-identical movement pattern under the US irradiation depending on their growing size. Understanding how bubbles of different sizes travel in the liquid medium would make it easier to determine whether that movement is effective in cleaning the membrane surface efficiently. According to our observations, small bubbles tend to move toward the US transducer at all US frequencies, as shown in Figure S.3 (a) Figure S.3 (b) where the frame in Figure S.3 (a) was captured before that in Figure S.3 (b). Those figures also show a single bubble grew as it traveled toward the US transducer. The upward movement of the small bubbles can also be seen in Figure S.3 (1 to 6 as time was advancing from the formation of the bubbles)

In fact, all bubbles smaller than the resonance size moved upward (toward the antinode). The bubble resonance size can be determined by the following equation [30]:

Table 2
Summary of results from images with minimum, averaged, and maximum numbers of bubbles at different US frequency (60 Watts).

		Average number of bubbles	Average bubble radius (μm)	Average variation of density (%)
Image with minimum number of bubbles per US duration at:	20 kHz	126	157	22.2
	28 kHz	495	16	1.1
	40 kHz	590	13	0.7
Image with average number of bubbles per US duration at:	20 kHz	176	134	22.4
	28 kHz	793	20	2.4
	40 kHz	808	20	2.2
Image with maximum number of bubbles per US duration at:	20 kHz	238	116	23.0
	28 kHz	962	20	2.9
	40 kHz	1091	24	4.3

$$f_r = \frac{1}{2\pi}\frac{1}{R_0}\sqrt{\frac{3\gamma\rho_{air}}{\rho_{water}}} \quad (1)$$

where f_r is the resonance frequency, R_0 the resonance radius, γ the specific heat ratio of air (C_p/C_v), ρ_{air} the density of air inside the bubbles, and ρ_{water} the density of water surrounding the bubbles.

Moreover, the velocity of moving bubbles was inversely proportional to their size; and hence, smaller bubbles moved faster and disappeared as they got close to the US transducer. The velocity of large bubbles was very slow such that they appeared to be stationary. It is worth mentioning that the majority of small bubbles are transient bubbles oscillating and traveling through the water medium. However, most of the large bubbles are stationary and stable bubbles oscillating at their positions or moving very slow. Fig. 10 (a) shows a frame of both the moving and stationary bubbles where Fig. 10 (b) shows the behaviour over time of both the transient and stable bubbles at the frequency of 20 kHz.

Table 4 presents the resonance (R_0) and average size (R_{avg}) of the created bubbles, as well as the velocity of moving bubbles at each US frequency. It was revealed that the mean bubble size was smaller than the resonance size at all US frequencies. The result of the velocity calculation also indicated that small bubble velocity increased from 36 μm/ms to 65 $\mu m/ms$ as the frequency increased from 20 kHz to 28 kHz. However, a further increase in US frequency from 28 kHz to 40 kHz, the velocity slightly decreased to 64μm/ms. This trend could be attributed to the changes in the average bubble size or the ratio of the average bubble size to the resonance bubble size (R_{avg}/R_0). It is evident that bubbles with the largest size and the highest R_{avg}/R_0 at 20 kHz moved slowest as compared with all other bubbles at 28 kHz and 40 kHz. It means bubbles close to the resonance size and the higher R_{avg}/R_0 have lower velocity compare to smaller bubbles.

From the results obtained and analyses presented in the previous section, it can be concluded that as the bubbles become larger, the travel velocity becomes slower towards the transducer. It appears that larger bubbles tend to stay at the lower level of the frames, where the membrane would be located. In this case, the energy released as a result of their explosions would help break the fouling layer. Moreover, the convective current, formed due to the larger bubbles' oscillation, would further remove the particles from the membrane surface. Bubbles larger than their resonance size were also observed in frames captured at 20 kHz. As expected, some of them stayed at the lower levels of the frames, and their distances from the US transducer did not change over the time (did not travel, only oscillated). However, a number of large stationary bubbles were also observed near the transducer. Although it seems more favourable to have bubbles close to the membrane (middle slice), those microbubbles were large enough to affect the flow underneath (over the membrane surface) and to create the convective current. Small bubble movement could also be beneficial for particle removal and surface cleaning. The small bubbles' movement toward the upper level can help to dislodge the particles by attaching to them and clearing them away from the surface.

Bubbles created at 28 kHz and 40 kHz were smaller than their resonance size and had a lower R_{avg}/R_0 ratio; thereby, those bubbles moved faster through the water medium towards the transducer compared to bubbles at 20 kHz. Therefore, it seems microbubbles at 28 kHz and 40 kHz can take the suspended particles away from the membrane surface much faster than those at 20 kHz and make larger contribution in fouling remediation. However, the US cleaning technique relies upon breaking the fouling layer with the help of turbulent flow and shear forces created by the large bubbles' oscillating or their explosion. The bubbles generated at 28 and 40 kHz were not large enough compared to those of 20 kHz. Thus, it seems bubbles release a lower amount of energy to the system, which is not favourable for the formation of eddy current within the water medium and for the fouling mitigation.

4.6. Microbubble growth pattern

Microbubble nuclei expand their initial size under US exposure and frequently oscillate to reach a maximum size. Microbubbles may continue their existence as stable bubbles, or they may collapse vigorously under some particular conditions. Bubble oscillation and bubble explosion lead to the formation of convective current and turbulent flow in liquid. As the bubbles grow and reach a larger size, the oscillation becomes stronger and the explosion takes place more vigorously; resulting in the creation of eddy current around those large bubbles. Thus, detailed information on how bubbles' size changes with time would help to understand the way microbubbles affect the fouling removal over the US exposure period.

The oscillation, growth, and movement of 22 representative bubbles at 20 kHz were monitored for 700 ms so to calculate their growth rate. Those 22 microbubbles were seen together for the first time in a frame captured 40 ms after imaging started. Microbubbles existed in the next 1400 frames (700 ms duration) captured by the camera, but hence, a few of them disappeared. Fig. 11 (a) and (b) show the bubbles at 40 ms and 740 ms of US exposure. The size (bubble radius) of 22 representative bubbles was measured over the period of 700 ms with the 100 ms interval. The bubble radius versus time plot is presented in Fig. 11 (c). After measuring the bubble size, bubble growth ratio (R_2/R_1, where R_1 is the initial bubble size at 40 ms and R_2 is the size at every 100 ms interval after) was calculated for each bubble. Different growth rates were

Table 3
Bubble dynamics at different distances from US transducer presented in Fig. 6.

US frequency	Average number of bubbles			Average bubble radius(μm)			Average variation of density (%)		
	Slice 1	Slice 2	Slice 3	Slice 1	Slice 2	Slice 3	Slice 1	Slice 2	Slice 3
20 kHz	45	67	61	149	126	106	7.1	7.7	5.4
28 kHz	305	346	102	17	21	16	0.6	1.1	0.2
40 kHz	309	325	125	15	21	18	0.5	1.0	0.3

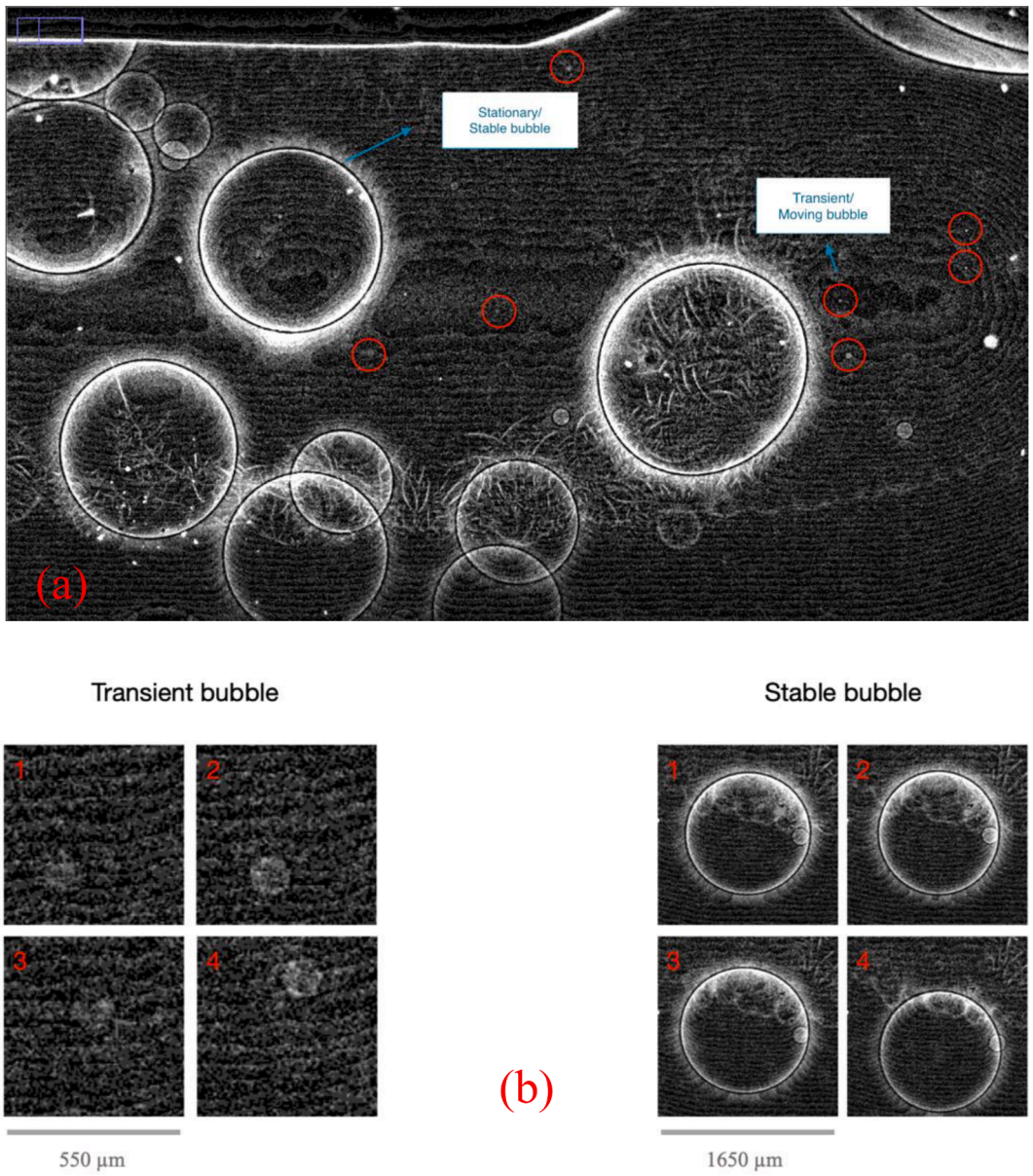

Fig. 10. a) Moving and stationary bubbles at 20 kHz, b) Behaviour of transient and stable bubbles at 20 kHz (4 consecutive frames).

Table 4
Bubble characteristics at different US frequencies at 60 Watts.

Frequency (kHz)	Resonance bubble radius (μm)	Average bubble radius (μm)	Velocity (μm/ms)	R_{avg}/R_0
20	150	135	36	0.9
28	107	20	65	0.2
40	75	20	64	0.3

obtained from different cavitational bubbles depending on their initial size. Thus, an average growth ratio for 22 measurements was calculated at each 100 ms interval. Afterward, the mean growth ratio over time was plotted and a polynomial equation was fitted to the data so to obtain a relationship between the growth ratio and exposure time, which is shown in Fig. 11 (d). Data fitting through the regression has a $R^2 = 0.989$. Result indicates an accurate correlation based on the regression coefficient.

All 22 microbubbles presented in Fig. 11 are large bubbles with $R > 10\ \mu m$. Thus, this growth pattern equation works for large bubbles ($R > 10\ \mu m$) captured between 40 ms and 740 ms of imaging. As it is evident, the mean growth ratio varies between 1 and 5 % in terms of the bubble radius (1–25 % in terms of the bubble projected area). Among all those representative bubbles, the maximum growth ratio recorded belongs to bubble 1 and it is 38 %, approximately. However, for small bubbles ($R < 10\ \mu m$), bubbles could expand up to 200 % from their initial size (the initial size was equal to the smallest size that could be captured by the camera detector ($R \cong 3\ \mu m$). It worth mentioning that bubble size reduction was also observed over the 700 ms of imaging due to the bubble oscillation. The results of the growth rate calculation revealed that large bubbles were mostly stable bubbles oscillating in water whilst, small bubbles were mostly transient bubbles with remarkable growth ratio.

5. Conclusions

Cavitation dynamics and detailed information of bubble characteristics were comprehensively studied using Synchrotron BMIT-BM 05B1-1 beamline. The optimized in-line PCI synchrotron X-ray imaging with

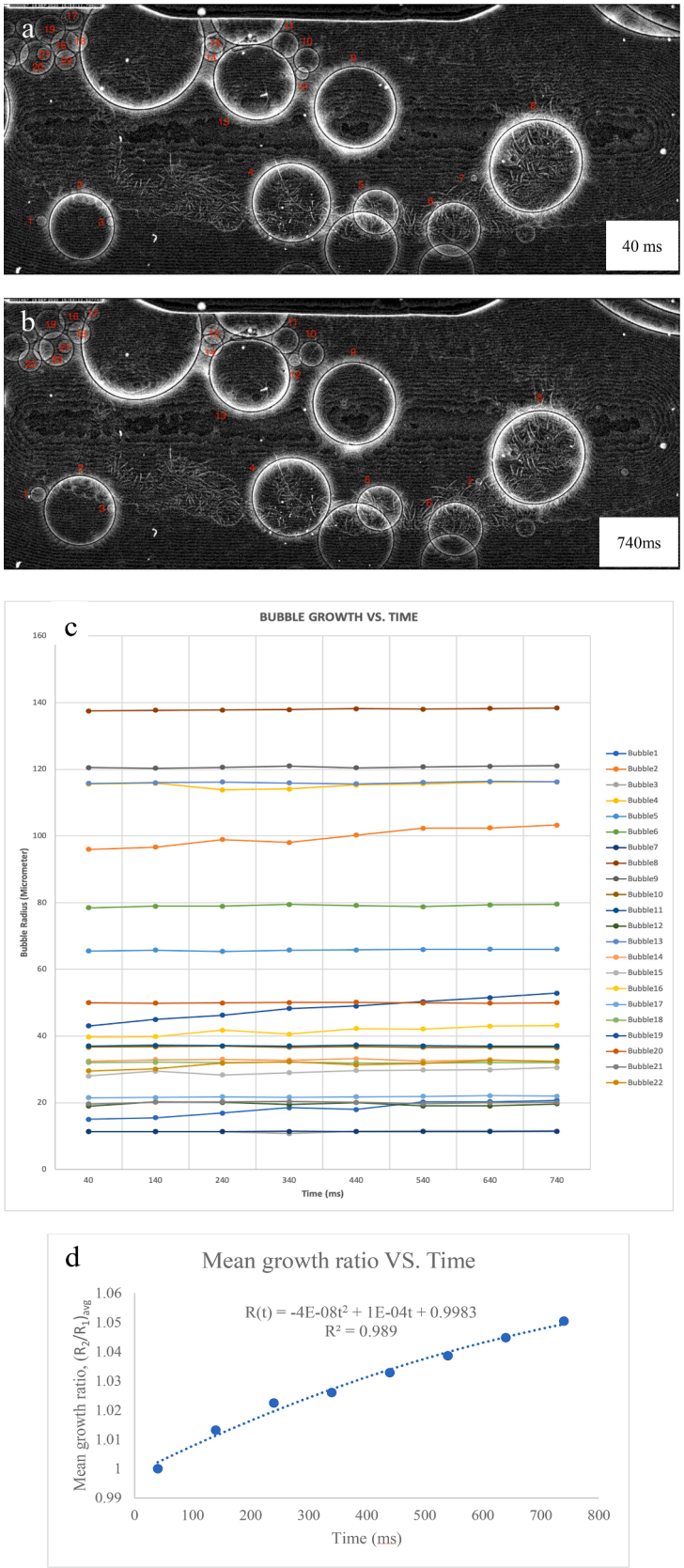

Fig. 11. Microbubble growth pattern at 20 kHz, a) initial bubble size, b) microbubbles after 700 ms, c) bubble size changes with time, d) the correlation between mean growth ratio and time.

high phase contract of gas/liquid was used to capture the moving and stationary microbubbles. Ultrasound experiments were performed at three different US frequencies of 20 kHz, 28 kHz, and 40 kHz with the US power of 60 W. High-quality images were obtained by optimizing the crucial parameters, including filtration unit design and material, selected beam, energy, and detector settings, SDD, camera speed, and the mode of imaging. A spectral energy setting was selected based on the radiation transmitted through the sample and pixel saturation values that achieved the best flux and imaging quality. A photon flux of $\sim 10^{13}$ photons/mm^2/s of white beam was used in this study. A total of 4000 projections/ 2 s (one image per 0.5 ms) were obtained. Bubble creation and its dynamic patterns under the US exposure were thoroughly monitored and analyzed using the captured images at CLS. Bubble characteristics in terms of the number, size, and the fraction of total area occupied by microbubbles, were quantified.

The results revealed that larger bubbles were created at a lower frequency, and their size was very close to their resonance size. The averaged bubble size at 20 kHz was about 135 μm while this value was only about 20 μm at 40 kHz ($R_{avg,20}/R_{avg,40} = 6.8$). The average number of bubbles, created under the US exposure, increased from 176 to 808 bubbles when the frequency increased from 20 kHz to 40 kHz. The averaged number and size of the bubbles created at a specific frequency did not change significantly with the US exposure time. It was observed that most bubbles were generated at the middle slice (1.734–3.072 mm away from the transducer) where the US field was observed. This could be an advantage for the membrane surface cleaning and particle removal., The velocity of bubbles relied on their size, such that small bubbles moved faster. It was observed that bubbles smaller than the resonance size traveled upward toward the US transducer. Bubbles larger than their resonance size seemed to be the stable bubbles oscillating in their position. The potential oscillation and explosion may lead to the formation of eddy current and shear force on the membrane surface, which would contribute in disrupting membrane fouling. A correlation of the growth rate for the large bubbles ($R > 10$ μm) at 20 kHz with the US exposure time was also developed. The maximum value for the mean growth rate was almost 5 % in terms of the bubble radius (25 % in terms of the bubble projected area).

The majority of large bubbles were stable bubbles with fairly constant size. On the other hand, small bubbles were transient bubbles moving through the liquid medium, and those bubbles could grow up to 200 % of their initial radius. Small bubbles moving upward can act as microstreamers. This is attributed to their potential attachment to the particles, carry them away from the membrane surface, and helping further with fouling removal. Further investigations on the effects of other operational parameters on microbubble dynamics and its influence on membrane fouling remediation efficiency are in progress.

CRediT authorship contribution statement

Masoume Ehsani: Formal Analysis, Writing – original draft. **Ning Zhu:** Investigation, Data curation, Writing – original draft, Review & editing. **Huu Doan:** Program Conceptualization, Writing – review & editing. **Ali Lohi:** Writing – review & editing. **Amira Abdelrasoul:** Synchrotron Conceptualization, Methodology, Data curation, Writing – original draft, Review & editing.

Declaration of Competing Interest

The authors declare that they have no known competing financial interests or personal relationships that could have appeared to influence the work reported in this paper.

Acknowledgments

The authors highly appreciate the Canadian Natural Sciences and Engineering Research Council (NSERC) for funding the project. Also, the authors would like to acknowledge the support offered at the Canadian Light Source (CLS), a national research facility at the University of Saskatchewan, which is supported by the Canada Foundation for Innovation (CFI), the Natural Sciences and Engineering Research Council (NSERC), the National Research Council (NRC), the Canadian Institutes of Health Research (CIHR), the Government of Saskatchewan, the University of Saskatchewan. The authors would like to thank Ryerson University and University of Saskatchewan. The authors would also like to express their gratitude to RLee Prokopishyn (University of Saskatchewan) for his much appreciated efforts on different CLS setup designs at the beamline hatch.

Data Availability Statement

Raw data generated at CLS beamline (images and videos); and the derived data supported the key findings of this study are available from the corresponding authors on reasonable request.

Appendix A. Supplementary data

Supplementary data to this article can be found online at https://doi.org/10.1016/j.ultsonch.2021.105697.

References

[1] J. Li, R.D. Sanderson, E.P. Jacobs, Ultrasonic cleaning of nylon microfiltration membranes fouled by Kraft paper mill effluent, J. Mem. Sci. 205 (2002) 247–257, https://doi.org/10.1016/S0376-7388(02)00121-7.
[2] S. Muthukumaran, K. Yang, A. Seuren, S. Kentish, M. Ashokkumar, G.W. Stevens, F. Grieser, The use of ultrasonic cleaning for ultrafiltration membranes in the dairy industry, Sep. & Puri. Tech. 39 (1-2) (2004) 99–107, https://doi.org/10.1016/j.seppur.2003.12.013.
[3] X. Li, J. Yu, A.G.A. Nnanna, Fouling mitigation for hollow- fiber UF membrane by sonication, Desalination 281 (2011) 23–29, https://doi.org/10.1016/j.desal.2011.07.036.
[4] K.M. Lee, H. Doan, F. Ein-Mozaffari, intermittent ultrasound-ssited ceramic membrane fouling control in ultrafiltration, Canadian. J. Chem. Eng. 98 (2020) 1648–1667, https://doi.org/10.1002/cjce.23777.
[5] H.W.D. Camara, H. Doan, A. Lohi, In-situ ultrasound-assisted control of polymeric membrane fouling, Ultrasonics 108 (2020) 106206–106219, https://doi.org/10.1016/j.ultras.2020.106206.
[6] S.R. Gonzalez-avila, F. Prabowo, A. Kumar, C. Ohl, Improved ultrasonic cleaning of membranes with tandem frequency excitation, J. Memb. Sci. 415 (2021) 776–783, https://doi.org/10.1016/j.memsci.2012.05.069.
[7] S. Muthukumaran, S. Kentish, S. Lalchandani, M. Ashokkumar, R. Mawson, G. W. Stevens, F. Grieser, The optimisation of ultrasonic cleaning procedures for dairy fouled ultrafiltration membranes, Ultrason. Sonochem. 12 (1-2) (2005) 29–35, https://doi.org/10.1016/j.ultsonch.2004.05.007.
[8] E. Alventosa-deLara, S. Barredo-Damas, M.I. Alcaina-Miranda, M.I. Iborra-Clar, Study and optimization of the ultrasound-enhanced cleaning of an ultrafiltration ceramic membrane through a combined experimental– statistical approach, Ultrason. Sonochem. 21 (3) (2014) 1222–1234, https://doi.org/10.1016/j.ultsonch.2013.10.022.
[9] N.V. Thombre, A.P. Gadhekar, A.V. Patwardhan, P.R. Gogate, Ultrasound induced cleaning of polymeric nano filtration membranes, Ultrason. Sonochem 62 (2019) 104891–104901, https://doi.org/10.1016/j.ultsonch.2019.104891.
[10] Z. Izadifar, G. Belev, M. Izadifar, Z. Izadifar, D. Chapman, Visualization of ultrasound induced cavitation bubbles using the synchrotron x-ray Analyzer Based Imaging technique, Phys. Med. Biol. 59 (23) (2014) 7541–7555, https://doi.org/10.1088/0031-9155/59/23/7541.
[11] T. Ding, S. Zhang, Q. Fu, Z. Xu, M. Wan, Ultrasound line-by-line scanning method of spatial-temporal active cavitation mapping for high-intensity focused ultrasound, Ultrasonics 54 (1) (2014) 147–155, https://doi.org/10.1016/j.ultras.2013.04.011.
[12] R.A. Roy, S.I. Madanshetty, R.E. Apfel, An acoustic backscattering technique for the detection of transient cavitation produced by microsecond pulses of ultrasound, J. Acoust. Soc. Am. 87 (6) (1990) 2451–2458, https://doi.org/10.1121/1.399091.
[13] Z. Izadifar, P. Babyn, D. Chapman, Ultrasound Cavitation/Microbubble Detection and Medical Applications, J. Med. Biol. Eng. 39 (3) (2019) 259–276, https://doi.org/10.1007/s40846-018-0391-0.
[14] Z. Izadifar, G. Belev, P. Babyn, D. Chapman, Application of analyzer based X-ray imaging technique for detection of ultrasound induced cavitation bubbles from a physical therapy unit, Biomed. Eng. Online 14 (2015) 1–12, https://doi.org/10.1186/s12938-015-0085-6.
[15] S.Y. Jung, H.W. Park, S.H. Park, S.J. Lee, Synchrotron x-ray imaging of acoustic cavitation bubbles induced by acoustic excitation, Meas. Sci. Technol. 28 (2017) 045301–045307, https://doi.org/10.1088/1361-6501/aa5e26.

[16] F. Arfelli, L. Rigon, R.H. Menk, Microbubbles as x-ray scattering contrast agents using analyzer-based imaging, Phys. Med. Biol. 55 (6) (2010) 1643–1658, https://doi.org/10.1088/0031-9155/55/6/008.
[17] T. P. Millard, M. Endrizzi, N. Everdell, L. Rigon, F. Arfelli, R. H. Menk, E. Stride, A. Olivo., Evaluation of microbubble contrast agents for dynamic imaging with x-ray phase contrast, Sci. Rep.,5 (2015) 1–9. https://doi.org/10.1038/srep12509.
[18] R. Tang, W.-M. Chai, F. Yan, G.-Y. Yang, K.-M. Chen, Molecular evaluation of thrombosis using X-ray phase contrast imaging with microbubbles targeted to P-selectin in mice, Eur. Radiol. 26 (9) (2016) 3253–3261, https://doi.org/10.1007/s00330-015-4129-x.
[19] D.a. Shu, B. Sun, J. Mi, P.S. Grant, A high-speed imaging and modeling study of dendrite fragmentation caused by ultrasonic cavitation, Metall. Mater. Trans. A Phys. Metall. Mater. Sci. 43 (10) (2012) 3755–3766, https://doi.org/10.1007/s11661-012-1188-3.
[20] J. Mi, D. Tan, T.L. Lee, In Situ Synchrotron X-ray Study of Ultrasound Cavitation and Its Effect on Solidification Microstructures, Metall. Mater. Trans. B Process Metall. Mater. Process. Sci. 46 (4) (2015) 1615–1619, https://doi.org/10.1007/s11663-014-0256-z.
[21] I. Tzanakis, W. W. Xu, G. S. B. Lebon, D. G. Eskin, K. Pericleous, P. D. Lee, In situ synchrotron radiography and spectrum analysis of transient cavitation bubbles in molten aluminium alloy, Phys. Procedia, 70 (2015) 841–845. https://doi.org/10.1016/j.phpro.2015.08.172.
[22] D. Tan, T.L. Lee, J.C. Khong, T. Connolley, K. Fezzaa, J. Mi, High-Speed Synchrotron X-ray Imaging Studies of the Ultrasound Shockwave and Enhanced Flow during Metal Solidification Processes, Metall. Mater. Trans. A Phys. Metall. Mater. Sci. 46 (7) (2015) 2851–2861, https://doi.org/10.1007/s11661-015-2872-x.
[23] H. Huang, D.a. Shu, Y. Fu, G. Zhu, D. Wang, A. Dong, B. Sun, Prediction of Cavitation Depth in an Al-Cu Alloy Melt with Bubble Characteristics Based on Synchrotron X-ray Radiography, Metall. Mater. Trans. A Phys. Metall. Mater. Sci. 49 (6) (2018) 2193–2201.
[24] W. Lu, N. Zhang, Z. Ding, F. Yang, Q. Hu, L. Zeng, J. Li, Bubble growth, intermetallic compounds dissolution and their interactions during heating of an Al-5wt.%Mn alloy by in-situ synchrotron radiography, J. Alloys Compd. 822 (2020) 153554, https://doi.org/10.1016/j.jallcom.2019.153554.
[25] I. Tzanakis, W.W. Xu, D.G. Eskin, P.D. Lee, N. Kotsovinos, In situ observation and analysis of ultrasonic capillary effect in molten alluminium, Ultrason. Sonochem. 27 (2015) 72–80, https://doi.org/10.1016/j.ultsonch.2015.04.029.
[26] Z. Li, Z. Xu, D. Zhao, S. Chen, J. Yan, Ultrasonic cavitation at liquid/solid interface in a thin Ga-In liquid layer with free surface, Ultrson. Sonochem. 71 (2021) 105356–105368, https://doi.org/10.1016/j.ultsonch.2020.105356.
[27] W.W. Xu, I. Tzanakis, P. Srirangam, W.U. Mirihanage, D.G. Eskin, A.J. Bodey, P. D. Lee, Synchrotron quantification of ultrasound cavitation and bubble dynamics in Al-10Cu melts, Ultrason. Sonochem. 31 (2016) 355–361, https://doi.org/10.1016/j.ultsonch.2016.01.017.
[28] H. Huang, D.a. Shu, Y. Fu, J. Wang, B. Sun, Synchrotron radiation X-ray imaging of cavitation bubbles in Al-Cu alloy melt, Ultrason. Sonochem. 21 (4) (2014) 1275–1278.
[29] C. Wang, T. Connolley, I. Tzanakis, D. Eskin, J. Mi, Characterization of ultrasonic bubble clouds in a liquid metal by synchrotron X-ray high speed imaging and statistical analysis, Materials.,13 (2020) 44-55. https://doi.org/10.3390/ma13010044.
[30] M. Minnaert, XVI. On musical air-bubbles and the sounds of running water, London, Edinburgh, Dublin Philos. Mag. J. Sci.16 (1993) 235–248, 1933.